Rapid leukocyte migration by integrin-independent flowing and squeezing

Tim Lämmermann[1], Bernhard L. Bader[3], Susan J. Monkley[4], Tim Worbs[5], Roland Wedlich-Söldner[2], Karin Hirsch[1], Markus Keller[3], Reinhold Förster[5], David R. Critchley[4], Reinhard Fässler[1] & Michael Sixt[1]

All metazoan cells carry transmembrane receptors of the integrin family, which couple the contractile force of the actomyosin cytoskeleton to the extracellular environment. In agreement with this principle, rapidly migrating leukocytes use integrin-mediated adhesion when moving over two-dimensional surfaces. As migration on two-dimensional substrates naturally overemphasizes the role of adhesion, the contribution of integrins during three-dimensional movement of leukocytes within tissues has remained controversial. We studied the interplay between adhesive, contractile and protrusive forces during interstitial leukocyte chemotaxis *in vivo* and *in vitro*. We ablated all integrin heterodimers from murine leukocytes, and show here that functional integrins do not contribute to migration in three-dimensional environments. Instead, these cells migrate by the sole force of actin-network expansion, which promotes protrusive flowing of the leading edge. Myosin II-dependent contraction is only required on passage through narrow gaps, where a squeezing contraction of the trailing edge propels the rigid nucleus.

The current model of metazoan cell migration is frequently described as a multistep cycle: F-actin polymerization at the cell front pushes out a membrane protrusion that subsequently becomes anchored to an extracellular substrate by transmembrane receptors of the integrin family. Integrins are dynamically coupled to the cytoskeleton and transduce the internal force that is generated when myosin II contracts the actin network. Contraction imposes retrograde pulling forces on the integrins, which in turn facilitates forward locomotion of the cell body[1–3]. The mammalian integrin family consists of 24 different functional heterodimers with individual binding specificities for cellular and extracellular ligands[4]. The integrin repertoire of each cell type defines which substrate it can use for this 'haptokinetic' (adhesion driven) mode of migration. Such intimate linkage between substrate-specific adhesion and migration restricts the migrating cells to preformed pathways, and thereby creates the determinism that is essential for many of the precise cell trafficking and positioning processes underlying compartmentalization and patterning during development and regeneration. As all mammalian cells with the exception of erythrocytes carry integrins on their surface, it is reasonable to assume that haptokinesis is a universal phenomenon[4,5].

Leukocytes are outstanding cells, as they are scattered throughout the body and have the potential to infiltrate any type of tissue. Rather than following exact routes and being restricted to specific compartments, leukocytes frequently undergo stochastic swarming with single cell migration velocities that are up to 100 times faster than mesenchymal and epithelial cell types[6,7]. What makes leukocytes so quick and flexible? In contrast to slow cells, migrating leukocytes undergo frequent shape changes and were therefore morphologically described as ''amoeboid''[8]. How these shape changes relate to actual locomotion is poorly investigated, and it is currently unknown if amoeboid migration represents a specialized strategy or just an accelerated variant of the above introduced migration paradigm that is only well established for slow cells. We therefore studied the inter-dependency of adhesion, protrusion and contraction in inflammatory cells. We demonstrate that integrin-mediated adhesion is only necessary to overcome tissue barriers like the endothelial layer, while interstitial migration is autonomous from the molecular composition of the extracellular environment. Such adhesion-independent migration is driven by protrusive flowing of the anterior actin network of the cell and supported by squeezing actomyosin contractions of the trailing edge to propel the rigid nucleus through narrow spaces.

Dendritic cells migrate without integrins

As a model system to study interstitial leukocyte migration *in vivo*, we focused on dendritic cells (DCs), phagocytes that reside within peripheral tissues such as skin. They become activated upon wounding or infection, sample antigens and quickly migrate via the afferent lymphatic vessels into the draining lymph node where they act as antigen presenting cells[9]. DC migration is primarily guided by the two chemokines CCL19 and CCL21; these are expressed in lymphatic endothelium and the lymph nodes' T-cell area, and bind the CC-chemokine receptor 7 (CCR7), which is upregulated on DCs upon activation[10].

Flow cytometric analysis of DCs generated from mouse bone-marrow-derived stem cells revealed expression of the β_1, β_2, β_7 and α_v integrin families (Fig. 1a). To investigate the role integrins play in DC migration *in vivo*, we used a combinatorial mouse genetics approach to delete all integrin heterodimers from the surface of DCs, thereby generating phenotypically normal pan-integrin-deficient (integrin$^{-/-}$) DCs (Fig. 1a, see Supplementary Material, Methods, and Supplementary Figs 1, 2, 4c). We co-injected 1:1 mixtures of differentially labelled integrin$^{-/-}$ and wild-type DCs into the dermis of mouse footpads and quantified their arrival in T-cell areas of the draining lymph nodes. Surprisingly, wild-type and integrin$^{-/-}$ DCs arrived and localized in the T-cell area in an indistinguishable manner (Fig. 1b, c, Supplementary Fig. 3), whereas CCR7$^{-/-}$ DCs, which cannot interpret the directional information, failed to enter the lymph node (Fig. 1c) as previously described[10]. We next targeted integrin functionality indirectly by deleting the talin1 gene in DCs

[1]Department of Molecular Medicine, [2]Junior Research Group Cellular Dynamics and Cell Patterning, Max Planck Institute of Biochemistry, 82152 Martinsried, Germany. [3]Department of Nutritional Medicine, Technische Universität München, Munich, 85350 Freising, Germany. [4]Department of Biochemistry, University of Leicester, Leicester LE1 9HN, UK. [5]Institute of Immunology, Hannover Medical School, 30625 Hannover, Germany.

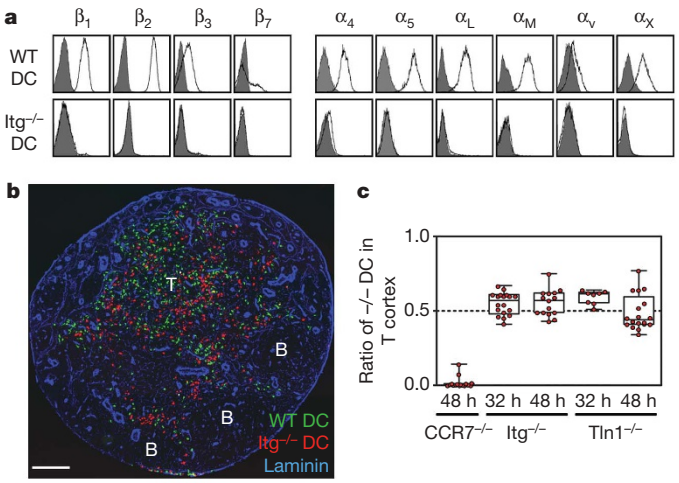

Figure 1 | Migration of integrin-deficient dendritic cells into lymph nodes. **a**, Flow cytometric analysis of integrin subunits of wild-type (WT) and integrin-deficient ($Itg^{-/-}$) dendritic cells (DCs) (integrin, unshaded; isotype control, grey-shaded). **b**, **c**, *In vivo* migration of DCs after subcutaneous injection into hind footpads of WT mice. At the time points indicated, arrival of differentially labelled DCs in the lymph node was analysed. **b**, Localization of DCs after 48 h. Composite of six separate images of a single lymph node. Scale bar, 200 μm; B, B-cell follicle; T, T-cell cortex. **c**, Quantitative histology. Dotted line at 0.5, 50% of DCs that migrated into the lymph node are knockout DCs; Tln1, talin1. Red dots indicate single experiments (1 lymph node); box shows median, 25%, 75% percentile; whiskers show minimum, maximum.

(Supplementary Fig. 4a). The interaction of talin1 with integrin cytoplasmic domains is required for integrin activation, ligand binding and coupling of F-actin to adhesion sites[11]. Accordingly, talin1 gene ablation in DCs did not affect the levels of integrin expression, but completely abolished their ability to bind ligands (Supplementary Fig. 4b–d). Again, arrival of $talin1^{-/-}$ DCs in lymph nodes did not significantly differ from wild-type DCs (Fig. 1c).

To allow for a detailed comparison of the cellular dynamics of wild-type and $integrin^{-/-}$ DCs within the different physiological environments of their migration route, we employed two *in situ* imaging approaches (Fig. 2). Representing the starting point of DC migration, the interstitial space of the dermis is dominated by fibrillar arrays of collagen bundles[12]. Using a newly developed set-up of *ex vivo* live cell imaging within explanted ear dermis, we could directly visualize DCs moving towards and entering the afferent lymphatic vessels by wide-field microscopy (Fig. 2b, c, Supplementary Fig. 5). Single cell tracking revealed no difference in the migratory behaviour of wild-type, $integrin^{-/-}$ and $talin1^{-/-}$ DCs (Fig. 2c, d).

The lymph node constitutes a fundamentally different environment for cellular migration, as it contains almost no freely accessible extracellular matrix molecules but is densely packed with lymphocytes and stroma cells[13,14]. To analyse the dynamics of intranodal DC migration from the subcapsular sinus towards the T-cell area, we employed a set-up of intravital two-photon microscopy of the popliteal lymph nodes[15]. Evaluating a range of motility parameters, including cell velocity, directional persistence, mean square displacement, motility coefficients and morphology, we found that the movement behaviour of wild-type and $integrin^{-/-}$ DCs was indistinguishable (Fig. 2e, f, Supplementary Videos 1–3, data not shown).

2D but not 3D migration is integrin-dependent

On their way into the lymph node, DCs do not cross significant tissue barriers, such as continuous endothelial or epithelial linings[12]. As these processes have been shown to be integrin-dependent[16], we also tested for extravasation of $integrin^{-/-}$ leukocytes from the blood stream into the inflamed dermis, and found that it was indeed abolished (Fig. 2g, Supplementary Fig. 6). This finding corroborates the extravasation model in which integrin-mediated tight immobilization of leukocytes to the luminal endothelial surface is necessary to counteract the shear forces imposed by the blood flow[16]. In line with this *in vivo* finding, we found that $integrin^{-/-}$ DCs were entirely unable to adhere to and migrate on two-dimensional (2D) substrates. Gravity was obviously not sufficient to confine the non-adherent cells to planar surfaces and allow the transduction of traction forces

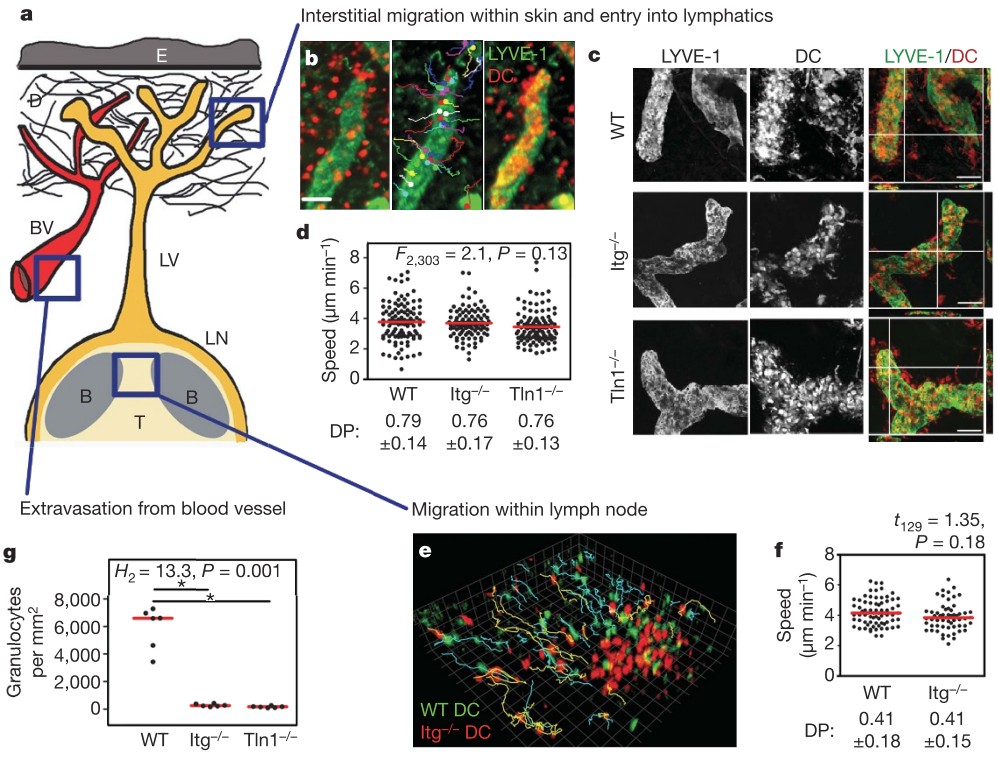

Figure 2 | Integrin-independent interstitial leukocyte migration *in vivo*. **a**, Scheme of the dendritic cell (DC) migration path from the skin via lymphatic vessels to the lymph node; B, B-cell follicle; BV, blood vessel; D, dermis; E, epidermis; LN, lymph node; LV, lymphatic vessel; T, T-cell cortex. **b–d**, Migration of DCs within the dermis of ear explants. **b**, Tracks of DCs (red) entering LYVE-1^{+} LVs (green). **c**, Confocal images of whole mount ear explants 2 h after addition of DCs (red). DCs locate within the lumen of LVs; all scale bars, 50 μm. **d**, Speed and directional persistence (DP, mean ± s.d.) of single cells (dots) for wild-type (WT), $integrin^{-/-}$ ($Itg^{-/-}$) and $talin1^{-/-}$ ($Tln1^{-/-}$) DCs. Red line, mean. **e**, **f**, Intravital two-photon microscopy. **e**, 3D tracking of WT (green, blue line) and $Itg^{-/-}$ (red, yellow line) DCs migrating in the interfollicular areas. **f**, Quantification of the average speed and DP (mean ± s.d.) of tracked single cells (dots). Red line, mean. **g**, Quantification of granulocytes that extravasated from blood into ear dermis ($n = 6$ for each mouse line). Red line, median. *$P < 0.05$ (post hoc).

(Fig. 3a, b, Supplementary Fig. 4d, Supplementary Video 4). We conclude that extravasation requires integrin-mediated adhesion.

To better mimic the interstitial microenvironment, we established chemotaxis assays within artificial three-dimensional (3D) matrices of fibrin (a ligand for β_2 and β_3 integrins) and collagen I (a ligand for several members of the β_1 integrin subfamily). In this system, DCs persistently migrated along soluble gradients of CCL19 and showed amoeboid morphology and velocities that were comparable to our (and previously published[17]) *in vivo* observations. In agreement with our *in vivo* data and in contrast to 2D migration, integrin$^{-/-}$ and talin1$^{-/-}$ DCs migrated with speed and directional persistence that were indistinguishable from wild-type cells (Fig. 3c, Supplementary Fig. 7a, Supplementary Video 5). We also observed integrin-independent migration for chemotaxing B cells and granulocytes, suggesting a broader prevalence of this functional principle (Fig. 3d, Supplementary Fig. 7b).

Functional dissociation of front and back

To mechanistically understand how cells can move in the absence of integrin-mediated traction forces, we compared the integrin-dependent movement pattern of fibroblasts with that of leukocytes and found a striking difference. Leading edge protrusions of fibroblasts translocated collagen fibres towards the cell body, indicating the presence of rearward pulling forces and demonstrating that protrusion, adhesion and contraction are tightly coupled in this cell type (Supplementary Video 6)[18,19]. In contrast, chemotaxing DCs protruded without signs of anterior pulling forces while the trailing edge displayed an irregularly alternating contractile pattern. Contraction was characterized by shrinkage of the cell rear with concomitant forward-streaming of cytoplasmic matter (Supplementary Video 7). When we dynamically visualized activated myosin II, the motor system mediating contraction[1,2,20], by time-lapse imaging of DCs expressing a myosin light chain–GFP fusion protein, we found accumulation at the cell rear during contractile phases (Fig. 4a, Supplementary Fig. 8a, Supplementary Video 8). During non-contractile phases, the trailing edge remained motionless and appeared to be passively dragged by the protruding cell front (Supplementary Video 7). These observations suggest that in contrast to slow moving cells, protrusion and contraction are spatio-temporally dissociated in leukocytes.

Receptor-mediated force transduction can only support forward movement if retrograde (contractile) but not anterograde (protrusive) forces are coupled to the environment[2,3]. To address how actomyosin contraction functionally contributes to leukocyte locomotion, we pharmacologically inhibited myosin II or its upstream-activator, Rho kinase. Irrespective of the presence of integrin function, either treatment severely reduced migration speeds of DCs, granulocytes and B cells (Fig. 4b, Supplementary Fig. 8e, data not shown). Nevertheless, the chemotactic gradient was still able to polarize the cell population. The leading edges of cells remained dynamic and protruded with normal speed towards the chemokine source. However, the cells were unable to move their trailing edges

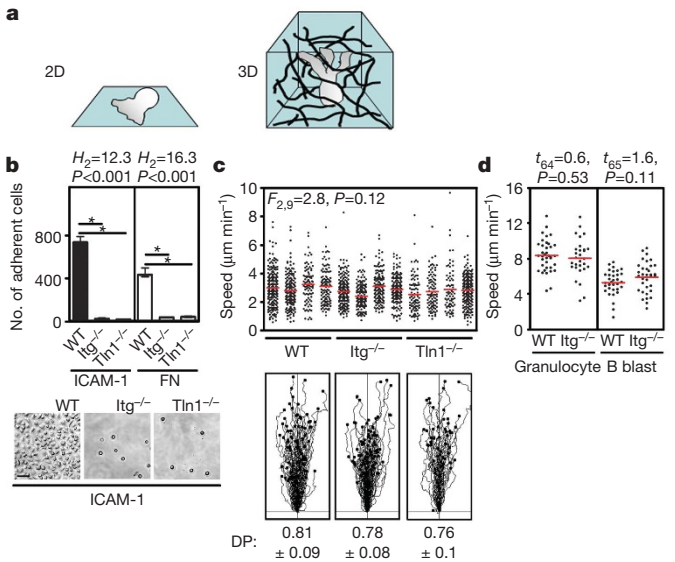

Figure 3 | Integrin-independent leukocyte migration in 3D networks *in vitro*. **a**, 2D adhesion versus 3D migration of DCs. **b**, 2D adhesion on ICAM-1 and fibronectin (FN) 1 h after LPS stimulation. Top, quantification of the number of adherent cells (ICAM-1, $n = 6$; FN, $n = 8$ for each experiment). Bars, median values with interquartile range, $^*P < 0.05$ (post hoc). Bottom, morphology of wild-type (WT), integrin$^{-/-}$ (Itg$^{-/-}$) and talin1$^{-/-}$ (Tln1$^{-/-}$) DCs. **c**, **d**, Velocities of chemotaxing leukocytes in 3D collagen matrices. **c**, Top, DCs (4 experiments per group); **d**, granulocytes, B cells. Dots, single cells; red line, mean. **c**, Bottom, single cell tracks of chemotaxing DCs; values indicate mean DP ± s.d.

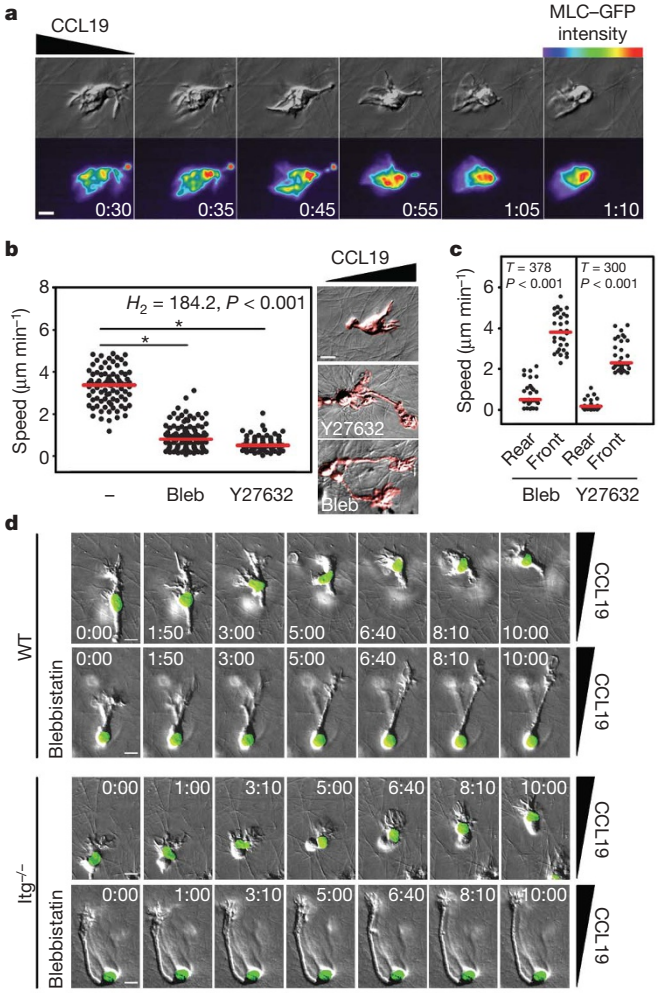

Figure 4 | Myosin II-dependent nuclear squeezing at the cell rear. **a**, Sequence of a myosin light chain (MLC)–GFP expressing wild-type (WT) dendritic cell (DC) migrating towards CCL19 in a 3D collagen gel; upper row, differential interference contrast (DIC) microscopy; lower row, MLC–GFP intensity profiles (encoded in pseudo-colours with red representing highest levels). Time in min:s. **b**, Left, velocities of single DCs (dots; red line, median), and right, DC morphology (coloured red, DIC microscopy), chemotaxing towards CCL19 in 3D collagen gels upon pharmacological inhibition. **c**, Speed of cell bodies (rear) versus cell protrusions (front) of DCs in the presence of inhibitor; red line, median. Bleb, blebbistatin; $^*P < 0.05$ (post hoc). **d**, **e**, Time-lapse sequence of a WT (**d**) and integrin$^{-/-}$ (**e**) DC either with (lower row) or without (upper row) blebbistatin; DIC microscopy, nuclei (green). Time in min:s; scale bars, 5 μm (**a**), 10 μm (**b**, **d**, **e**).

(Fig. 4b–e, Supplementary Fig. 8b–d, Supplementary Video 9). This functional dissociation between front and back caused up to 30-fold cell elongation, and demonstrates that the leading edge migrates autonomously and without a need for receptor-mediated coupling of contractile forces to the extracellular matrix.

Trailing edge contraction propels the nucleus

How does trailing edge contraction contribute to cell body locomotion? In fibroblasts and leukocytes moving on 2D substrates, actomyosin contraction at the back is required to disassemble receptor binding-sites and subsequently retract the membrane[2,21,22]. Hence, blocking contraction causes membrane tethers at the trailing edge. Consistent with an adhesion-independent migration mode, we could not observe membrane tethers in myosin II-inhibited leukocytes migrating in 3D gels. We considered that the elongated phenotype with its rounded back was caused by the inability to move an internal resistance through narrow gaps within the gel. As the nucleus is the least elastic cellular compartment[23], we visualized DNA within chemotaxing DCs and granulocytes. In untreated cells, we observed continuous shape changes of nuclei, indicating deformation forces, while upon myosin II inhibition, spherical nuclei were immobilized at the rear ends of the cells (Figs 4d, e, Supplementary Fig. 8b–d, Supplementary Videos 10, 11).

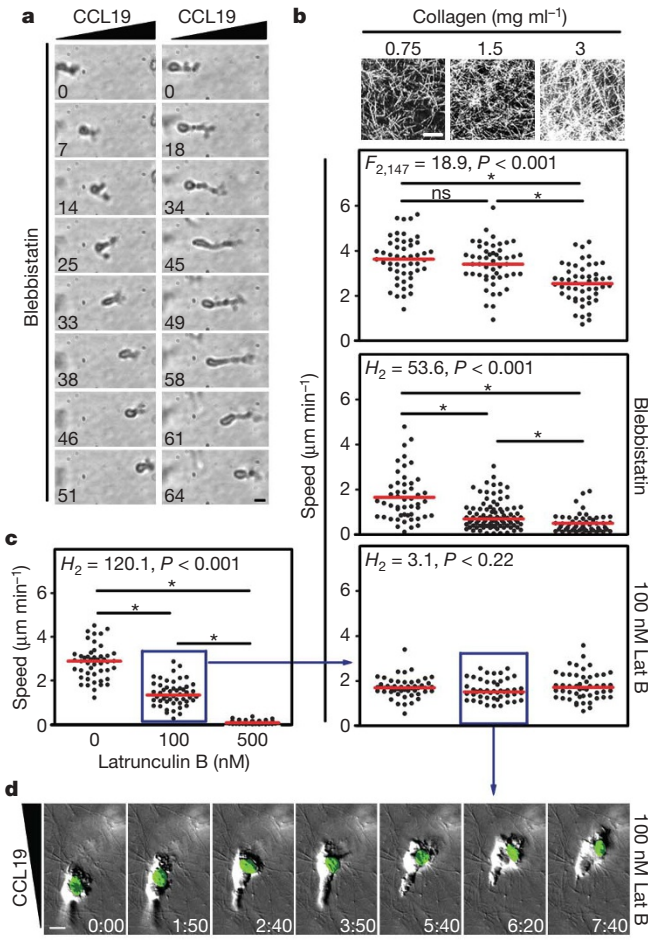

Figure 5 | Myosin II-independent protrusive migration of dendritic cells. **a**, Two types of residual migration of wild-type (WT) dendritic cells (DCs) treated with blebbistatin in a standard 3D collagen gel. DCs either drag the nucleus behind with elongated appearance and low speed (right column) or appear morphologically normal with high speed (left column). Time in min. **b**, Top panel, confocal reflection microscopy of 3D collagen networks of different densities. Lower panels, velocities of single chemotaxing WT DCs (dots) in collagen gels with varying densities. Upper graph, no inhibitor; red line, mean. Middle graph, blebbistatin; red line, median. Bottom graph, 100 nM latrunculin B (partial actin depolymerization); red line, median. **c**, Velocity of single WT DCs (dots) in the presence of different concentrations of latrunculin B (1.6 mg ml^{-1} collagen); red line, median. In **b** and **c**, $^*P < 0.05$ (post hoc). **d**, Time-lapse sequence of a 100 nM latrunculin B-treated WT DC; DIC microscopy, nuclei (green). Time, min:s. Blue boxes (in **b** and **c**) highlight experimental conditions that were used for follow-up experiments indicated by the blue arrow. Scale bars: 10 μm (**a**, **d**), 50 μm (**b**).

Protrusion drives basal locomotion

Although 'locked' nuclei caused migration arrest in most cells, a few still showed locomotion. This residual migration was often characterized by cell body elongation and dragging of the nucleus (Fig. 5a, Supplementary Video 12). Such non-contractile movement was in line with our previous observations showing motile phases in the absence of trailing edge contractions. We hypothesized that such myosin II-independent migration might occur in areas of the collagen gel where external resistance was low due to increased spacing of the collagen fibres. To establish the relationship between internal contractile force and external resistance, we analysed DC chemotaxis in collagen gels of varying fibre spacing (Fig. 5b). In all collagen densities, myosin II-inhibited DCs were slower than untreated cells but importantly, they 'caught up' at lowest gel densities (Fig. 5b, Supplementary Video 13). A comparison of instantaneous velocities further showed that myosin II inhibition did not prevent DCs from reaching the same peak values as untreated cells (Supplementary Fig. 9a–c).

We conclude that, in contrast to the 'blebbing' model of amoeboid cell migration[24], cortical actin network contraction does not mediate locomotion itself but rather facilitates a protrusive mode of migration in confined environments where protrusion alone is unable to act against counter-forces. So in constricted areas, the cell overcomes internal and external resistance (rigidity of the nucleus and fibre density) by contraction (myosin II). Contractile force deforms the resistance and facilitates a purely protrusive mode of migration.

To challenge the concept of protrusive movement, we treated chemotaxing DCs with latrunculin B, which interferes with actin polymerization by depleting the pool of available functional G-actin monomers[25]. We found that this treatment reduced cell migration velocity in a dose-dependent manner (Fig. 5c). At intermediate concentrations, the trailing edge remained contractile and the nucleus was 'pushed' to the cell front (Fig. 5d, Supplementary Video 14). Consistent with a model where protrusion determines the speed of cell migration while contraction is only activated to overcome external resistances, the speed reduction of latrunculin B-treated cells was independent of gel density (Fig. 5b, c).

Discussion

We show that leukocytes migrate in the absence of specific adhesive interactions with the extracellular environment. This subversion of the metazoan principle makes them autonomous from the tissue context, and allows them to quickly and flexibly navigate through any organ without adaptations to alternating extracellular ligands. This strategy is in stark contrast to the haptokinetic migration principle that leads along preformed pathways and therefore promotes deterministic positioning. Adhesion independency better suits stochastic movement or chemotaxis where cells randomly migrate or follow soluble cues. Astonishingly, the protrusive flow of F-actin appears sufficient to drive rapid leukocyte locomotion in environments with large pore-size. This resembles the locomotion principle of nematode sperm cells that is entirely driven by treadmilling polymers of major sperm protein[26]. Only in narrow areas do leukocytes activate the contractile module to squeeze and propel the internal resistance of the nucleus in a manner resembling neuronal nucleokinesis[27]. This 'flowing and squeezing' migration model fulfils a central requirement for immune cell movement: the pericellular environment is transiently deformed but never digested[28] or

otherwise permanently remodelled which avoids 'collateral damage', caused by infiltrating cells.

The fact that leukocytes are able to move autonomously generates a new level of regulatory possibilities. Because surface bound chemokines and other immobilized extracellular signals do trigger integrin affinity[16] (unlike soluble chemokines), leukocyte integrins should no longer be viewed as force transducers during locomotion but as switchable immobilizing anchors that stop, slow down or confine high intrinsic motility to specifically assigned surfaces[29,30]. The role of integrins is therefore mostly to mediate retention, invasion, cell–cell communication and cell–cell adhesion[31].

METHODS SUMMARY

Generation of integrin-deficient leukocytes. Integrins and talin1 were targeted by generating mice with the genotype $\alpha_v^{flox/flox}$ (Supplementary Fig. 1), $\beta_1^{flox/flox}$ (ref. 32), $\beta_2^{-/-}$ (ref. 33), $\beta_7^{-/-}$ (ref. 34), $Mx1Cre^{+/-}$ (ref. 35) and $talin1^{flox/flox}$ (ref. 36), $Mx1Cre^{+/-}$, respectively. Cre expression in the haematopoietic system was induced by intraperitoneal injection of 250 μg Poly (I)·Poly (C) (Amersham Biosciences). 10–14 d after knockout induction DCs were generated from bone marrow suspension and matured with lipopolysaccharide (LPS). The DC culture was depleted for granulocytes and remaining integrin-positive contaminants by magnetic sorting (Miltenyi Biotech). DCs used for migration assays were >99% enriched for β_1 and α_v integrin knockout cells.

***In situ* live cell imaging.** For dermal *ex vivo* microscopy, mouse ears were mechanically separated in dorsal and ventral halves, fluorescently stained with LYVE-1 antibody and immobilized with the epidermal side down. The dermis was overlaid with fluorescently labelled DCs and time lapse movies were recorded with an automated Leica MZ 16 FA stereomicroscope (Visitron Systems).

***In vitro* 3D chemotaxis assays.** Cells were suspended in PureCol (INAMED) and cast in custom built migration chambers (standard collagen concentration: 1.6 mg ml^{-1}). After polymerization, gels were overlaid with culture medium containing the chemoattractant (CCL19, C5a and CXCL13 for DCs, granulocytes and B cells, respectively) and subsequently imaged using wide-field fluorescence video microscopes with differential interference contrast (Zeiss). For nucleus visualization, SYTO-dyes (Invitrogen) were used. For visualization of myosin light chain, DCs were nucleofected using Amaxa technology. Inhibitors were titrated and used 50 μm blebbistatin (Sigma) and 30 μm Y27632 (Calbiochem).

Statistical analysis. *t*-tests and analysis of variance (ANOVA) were performed after data were confirmed to fulfil the criteria of normal distribution and equal variance, otherwise Kruskal–Wallis tests or Mann–Whitney U-tests were applied. If overall ANOVA or Kruskal–Wallis tests were significant, we performed a post hoc test. Analyses were performed with Sigma Stat 2.03. For further statistical details, see Supplementary Table.

Full Methods and any associated references are available in the online version of the paper at www.nature.com/nature.

Received 22 November 2007; accepted 6 March 2008.

1. Giannone, G. *et al.* Lamellipodial actin mechanically links myosin activity with adhesion-site formation. *Cell* **128,** 561–575 (2007).
2. Lauffenburger, D. A. & Horwitz, A. F. Cell migration: A physically integrated molecular process. *Cell* **84,** 359–369 (1996).
3. Mitchison, T. J. & Cramer, L. P. Actin-based cell motility and cell locomotion. *Cell* **84,** 371–379 (1996).
4. Hynes, R. O. Integrins: Bidirectional, allosteric signaling machines. *Cell* **110,** 673–687 (2002).
5. Hynes, R. O. & Zhao, Q. The evolution of cell adhesion. *J. Cell Biol.* **150,** 89–96 (2000).
6. Friedl, P. Prespecification and plasticity: Shifting mechanisms of cell migration. *Curr. Opin. Cell Biol.* **16,** 14–23 (2004).
7. Pittet, M. J. & Mempel, T. R. Regulation of T-cell migration and effector functions: Insights from *in vivo* imaging studies. *Immunol. Rev.* **221,** 107–129 (2008).
8. de Bruyn, P. P. H. The amoeboid movement of the mammalian leukocyte in tissue culture. *Anat. Rec.* **95,** 117–192 (1946).
9. Reis e Sousa, C. Dendritic cells in a mature age. *Nature Rev. Immunol.* **6,** 476–483 (2006).
10. Förster, R. *et al.* CCR7 coordinates the primary immune response by establishing functional microenvironments in secondary lymphoid organs. *Cell* **99,** 23–33 (1999).
11. Calderwood, D. A. & Ginsberg, M. H. Talin forges the links between integrins and actin. *Nature Cell Biol.* **5,** 694–697 (2003).
12. Stoitzner, P., Pfaller, K., Stössel, H. & Romani, N. A close-up view of migrating Langerhans cells in the skin. *J. Invest. Dermatol.* **118,** 117–125 (2002).
13. Gretz, J. E., Anderson, A. O. & Shaw, S. Cords, channels, corridors and conduits: Critical architectural elements facilitating cell interactions in the lymph node cortex. *Immunol. Rev.* **156,** 11–24 (1997).
14. Lämmermann, T. & Sixt, M. The microanatomy of T-cell responses. *Immunol. Rev.* **221,** 26–43 (2008).
15. Mempel, T. R., Henrickson, S. E. & Von Andrian, U. H. T-cell priming by dendritic cells in lymph nodes occurs in three distinct phases. *Nature* **427,** 154–159 (2004).
16. Alon, R. & Dustin, M. L. Force as a facilitator of integrin conformational changes during leukocyte arrest on blood vessels and antigen-presenting cells. *Immunity* **26,** 17–27 (2007).
17. Lindquist, R. L. *et al.* Visualizing dendritic cell networks *in vivo*. *Nature Immunol.* **5,** 1243–1250 (2004).
18. Meshel, A. S., Wei, Q., Adelstein, R. S. & Sheetz, M. P. Basic mechanism of three-dimensional collagen fibre transport by fibroblasts. *Nature Cell Biol.* **7,** 157–164 (2005).
19. Vanni, S., Lagerholm, B. C., Otey, C., Taylor, D. L. & Lanni, F. Internet-based image analysis quantifies contractile behavior of individual fibroblasts inside model tissue. *Biophys. J.* **84,** 2715–2727 (2003).
20. Medeiros, N. A., Burnette, D. T. & Forscher, P. Myosin II functions in actin-bundle turnover in neuronal growth cones. *Nature Cell Biol.* **8,** 215–226 (2006).
21. Hogg, N., Laschinger, M., Giles, K. & McDowall, A. T-cell integrins: More than just sticking points. *J. Cell Sci.* **116,** 4695–4705 (2003).
22. Morin, N. A. *et al.* Nonmuscle myosin heavy chain IIA mediates integrin LFA-1 de-adhesion during T lymphocyte migration. *J. Exp. Med.* **205,** 195–205 (2008).
23. Hu, S., Chen, J., Butler, J. P. & Wang, N. Prestress mediates force propagation into the nucleus. *Biochem. Biophys. Res. Commun.* **329,** 423–428 (2005).
24. Paluch, E., Sykes, C., Prost, J. & Bornens, M. Dynamic modes of the cortical actomyosin gel during cell locomotion and division. *Trends Cell Biol.* **16,** 5–10 (2006).
25. Morton, W. M., Ayscough, K. R. & McLaughlin, P. J. Latrunculin alters the actin-monomer subunit interface to prevent polymerization. *Nature Cell Biol.* **2,** 376–378 (2000).
26. Bottino, D., Mogilner, A., Roberts, T., Stewart, M. & Oster, G. How nematode sperm crawl. *J. Cell Sci.* **115,** 367–384 (2002).
27. Schaar, B. T. & McConnell, S. K. Cytoskeletal coordination during neuronal migration. *Proc. Natl Acad. Sci. USA* **102,** 13652–13657 (2005).
28. Wolf, K., Müller, R., Borgmann, S., Bröcker, E. B. & Friedl, P. Amoeboid shape change and contact guidance: T-lymphocyte crawling through fibrillar collagen is independent of matrix remodeling by MMPs and other proteases. *Blood* **102,** 3262–3269 (2003).
29. Auffray, C. *et al.* Monitoring of blood vessels and tissues by a population of monocytes with patrolling behavior. *Science* **317,** 666–670 (2007).
30. Phillipson, M. *et al.* Intraluminal crawling of neutrophils to emigration sites: A molecularly distinct process from adhesion in the recruitment cascade. *J. Exp. Med.* **203,** 2569–2575 (2006).
31. Sixt, M., Bauer, M., Lämmermann, T. & Fässler, R. Beta1 integrins: Zip codes and signaling relay for blood cells. *Curr. Opin. Cell Biol.* **18,** 482–490 (2006).
32. Potocnik, A. J., Brakebusch, C. & Fässler, R. Fetal and adult hematopoietic stem cells require beta1 integrin function for colonizing fetal liver, spleen, and bone marrow. *Immunity* **12,** 653–663 (2000).
33. Wilson, R. W. *et al.* Gene targeting yields a CD18-mutant mouse for study of inflammation. *J. Immunol.* **151,** 1571–1578 (1993).
34. Wagner, N. *et al.* Critical role for beta7 integrins in formation of the gut-associated lymphoid tissue. *Nature* **382,** 366–370 (1996).
35. Kühn, R., Schwenk, F., Aguet, M. & Rajewsky, K. Inducible gene targeting in mice. *Science* **269,** 1427–1429 (1995).
36. Petrich, B. G. *et al.* Talin is required for integrin-mediated platelet function in hemostasis and thrombosis. *J. Exp. Med.* **204,** 3103–3111 (2007).

Supplementary Information is linked to the online version of the paper at www.nature.com/nature.

Acknowledgements We thank S. Cremer for help with statistical analysis, Z. Werb and P. Friedl for critical reading of the manuscript, and M. Bauer for technical support. This work was financed by the German Research Foundation (DFG), the Austrian Science Foundation (FWF) and the Max Planck Society. Work in D.R.C.'s laboratory was supported by the Wellcome Trust.

Author Contributions T.L. and M.S. designed and performed the experiments and analysed the data. M.S. wrote the paper. T.W. and R.Fö. performed intravital microscopy in lymph nodes. B.L.B. and M.K. generated the integrin α_v mouse. S.J.M. and D.R.C. generated the talin1 mouse. R.Fä. generated the integrin β_1 and the quadruple integrin knockout mouse and provided general support. K.H. assisted with experiments. R.W.S. contributed to data analysis and experimental design.

Author Information Reprints and permissions information is available at www.nature.com/reprints. Correspondence and requests for materials should be addressed to M.S. (sixt@biochem.mpg.de).

METHODS

Generation of integrin $\alpha_v^{+/flox}$ mice. To generate a conditional floxed α_v allele, a targeting vector spanning 8.2 kb of the murine α_v *integrin* locus[37] was constructed. First, the 2.2 kb genomic subclone pXB2.2 encoding the 5′ upstream region, exon 1 and part of the intron 1 of the α_v gene was used to introduce two *loxP*-sites. The 5′-*loxP1*-site including an EcoRI-restriction site to facilitate the identification of the targeted locus was cloned into the HindIII-site in the 5′-upstream region (nucleotide position, nt-pos., –310) of the α_v gene. The 3′-*loxP2*-site was introduced into the BamHI-site in intron 1 (nt-pos. +528). The genomic subclone pBS6 harbouring this BamHI-site at its 5′-end and ~6 kb 3′-downstream intron 1 sequences was used to clone a *pgk-neo;pgk-tk*-tandem gene selection-cassette (*neoTK*) flanked by two *frt*-sites (provided by G. R. Martin) into the BamHI-site. These two modified genomic regions of the α_v gene were then fused at the corresponding BamHI-site to obtain the α_v gene targeting vector. ES cell transfection, selection and screening was carried out as described[37] except that R1 ES cells[38] were used. Homologously targeted clones were identified by Southern blotting of EcoRI- or BamHI-digested DNA with 5′- or 3′-external probes A or B, respectively. To excise the neoTK selection cassette, targeted ES cells (*flneoTK*) were transiently transfected with the *CAGGS-FLPe*-expression construct[39] (provided by A. F. Stewart) and counterselected with ganciclovir. Loss of the selection cassette in the α_v floxed allele was then confirmed by Southern blotting. ES cell clones were injected into blastocysts of C57Bl/6 mice, and resulting germline transmitting male chimaeras were mated to C57Bl/6 females to generate heterozygous floxed α_v mice and wild-type F1 mice following protocols as described[37]. Two independent lines carrying the $\alpha_v^{+/flox}$ allele were established and initially maintained on a 129SV/C57BL/6 mixed background. $\alpha_v^{+/flox}$ and $\alpha_v^{flox/flox}$ mice show no obvious phenotype. Southern blot and PCR analyses: wild-type and mutant α_v alleles were assessed by Southern blot hybridization and/or PCR from DNA isolated from ES cells, mouse tail biopsies or from yolk sacs of embryos as described[37]. In brief, 10 μg of genomic DNA was digested with EcoRI or BamHI and analysed using radiolabelled 5′-external probe A (419 bp-EcoRI/XbaI DNA-fragment) or a 3′-external probe B (690 bp-SphI/EcoRI DNA-fragment), respectively (see Supplementary Fig. 1). Genomic DNA digested with EcoRI was used to confirm the presence or absence of the selection cassette with probe C encoding a 800 bp-PstI fragment of the neomycin-resistance gene. For genotyping wild-type (WT, +) and floxed α_v allele (flox) as well as the *cre*-mediated knockout allele ($\alpha_v^{\Delta ex1}$), PCR amplifications with genomic DNA and the specific primer set (see below) were performed. The positions of the primers are located in close vicinity to the *loxP*-sites. PCR amplifications using *Taq*-polymerase and standard reaction buffer adjusted to a final concentration of 1 mM $MgCl_2$ were carried out as follows. PCR samples were initially denatured at 94 °C for 3 min, followed by 35 cycles of amplification (94 °C for 1 min, 60 °C for 2 min, 72 °C for 3 min), and a final 10 min extension at 72 °C followed. PCR amplification products were separated through agarose gel electrophoresis. The allele-specific primer sequences, pairs and orientation (forward, Fw; reverse, Rev), the primer pairs and their corresponding PCR-product sizes are as follows: Primer-set (F30: 5′-AGGATGGAAGGGGAGGGAAATG-3′ (Fw; WT), F20: 5′-CTTGACCGCAA-GCGCACAGCACAG-3′ (Fw; WT), I2: 5′-CTGGATGCTGAGTGTCAGGT-3′ (Rev; WT)), PCR products (F20/I2: 499 bp (wild-type α_v allele, WT); F20/I2: 614 bp (floxed α_v allele, α_v^{flox}); F30/I2: 339 bp (*cre*-mediated α_v knockout allele, $\alpha_v^{\Delta ex1}$)).

Mouse strains. Mice with constitutive deletions of integrin β_7, integrin β_2, CCR7 and conditional $\beta_1^{flox/flox}$ mice were described[10,32–34]. All mice were kept on a mixed 129SV/C57BL/6 genetic background. The integrin targeted strains were inter-crossed with Mx1Cre transgenic mice to generate $\alpha_v^{flox/flox}$, $\beta_1^{flox/flox}$, $\beta_2^{-/-}$, $\beta_7^{-/-}$, $Mx1Cre^{+/-}$ animals. $Talin1^{flox/flox}$ mice[36] were crossed with Mx1Cre transgenic mice to obtain $talin1^{flox/flox}$, $Mx1Cre^{+/-}$ mice. All control animals were on a mixed 129SV/C57BL/6 genetic background. The mice were bred in a conventional animal facility at the Max Planck Institute of Biochemistry, and according to the local regulations.

Induction of the haematopoietic knockout. At an age between 8 and 12 weeks, mice of the desired genotype received a single intraperitoneal injection of 250 μg Poly (I)·Poly (C) (Amersham Biosciences), diluted in 0.5 ml phosphate buffered saline (PBS). Mice were killed 10–14 d after injection and knockout efficiency of haematopoietic precursors was estimated by flow cytometric analysis of peripheral blood platelets[40]. Bone marrow (BM) of mice with >85% integrin β_1-negative platelets was processed for dendritic cell (DC) culture or cell isolation. Platelet knockout efficiencies usually corresponded with knockout efficiencies of DCs and granulocytes, whereas peripheral B cells frequently showed lower efficiency.

Cell generation, separation and purification. DCs were generated from flushed BM suspension as described previously[41]. At day 8–10 of culture, 200 ng ml^{-1} LPS (Sigma-Aldrich; *E. coli* 0127:B8) was added overnight and the pan-integrin-deleted DCs were subsequently depleted of remaining $Gr\text{-}1^+$ and integrin β_1^+ contaminants. For depletion, cells were incubated with biotinylated antibodies against Gr-1 (RB6-8C5) and integrin β_1 (Ha2/5) (both BD Pharmingen), followed by streptavidin-microbead separation according to the manufacturers protocol (Miltenyi Biotech). The negatively selected DCs used for migration assays were >99% enriched for β_1 integrin knockout cells and β_1-deficient cells were always 100% deleted for integrin α_v. After enrichment the cells are referred to as $integrin^{-/-}$ DCs. $Talin1^{-/-}$ DCs were generated identically and depleted of $Gr\text{-}1^+$ contaminants. To determine knockout efficiencies, DC lysates were loaded on 12–15% gradient gels for electrophoresis under reduced conditions and western blotting. Talin was detected with mouse anti-pan-talin antibody (T3287, Sigma), and the loading control was performed with rabbit anti-mouse actin antibody (A2066, Sigma). Integrin β_1 was detected with the rabbit polyclonal anti-integrin β_1 antibody 1244[42]. Integrin α_v was detected with a rabbit polyclonal anti-integrin α_v antibody (Chemicon). Bound primary antibodies were detected with anti-mouse or anti-rabbit horse radish peroxidase (HRP) or anti-rabbit HRP (both Bio-Rad) as secondary antibodies, respectively. DCs with no detectable talin stain were chosen for experiments, guaranteeing that the cells were deleted for talin1 and that talin2 was neither expressed nor induced as a compensation mechanism in DCs. Granulocytes were isolated by staining whole bone marrow suspension with anti-Gr-1 PE or anti-Gr-1 PE/anti-β_1 FITC and subsequent fluorescent activated cell sorting using a FACSAria (BD Biosciences), revealing >96% purity. Before incorporation into the gels, granulocytes were treated for 30 min with 20 ng ml^{-1} TNF-α (Roche) at 37 °C. B lymphoblasts were generated by mincing spleens through a 70 μm nylon cell strainer (BD Pharmingen), lysing erythrocytes with ACK lysis buffer (0.15 M NH_4Cl, 1 mM $KHCO_3$, and 0.1 mM EDTA), and subsequent magnetic cell sorting (MACS) with mouse CD43 MicroBeads on LS columns (Miltenyi). The negatively sorted B cells were stimulated with 10 μg ml^{-1} LPS (Sigma) for 72 h at 37 °C, 5% CO_2. Streptavidin-microbead separation of integrin β_1^+ cells (see DCs) revealed >98% pan-integrin-deficient B lymphoblasts that we refer to as $integrin^{-/-}$ B lymphoblasts.

Flow cytometry. Mature DCs were identified as $CD11c^+$, $MHCII^{high}$ cells for wild-type and talin1-deficient cells. For $integrin^{-/-}$ cells, $MHCII^{high}$ cells corresponded to mature DCs as they carried enhanced levels of maturation markers CD86 and CD40. B lymphoblasts were identified as $B220^+$ cells, granulocytes as $Gr\text{-}1^+$ cells. Employed antibodies were against the mouse antigens: Gr-1 biotin and PE (RB6-8C5), B220 FITC (RA3-6B2), CD11c FITC and biotin (HL3), I-A/I-E biotin (2G9) and I-A/I-E PE (M5/114.15.2) (all from BD Pharmingen). For integrin expression profiles, the above cell markers were combined with antibodies raised against the mouse integrin chains: α_2 FITC (Ha 1/29), α_{IIB} FITC (MWReg30), α_M PE (M1/70), α_4 PE (9C10), α_5 PE (5H10-27), α_6 PE (GoH3), α_E PE (M290), α_v (RMV-7), β_1 biotin (Ha2/5), β_2 biotin (C71/16), β_3 biotin (2C9.G2), β_7 biotin (2C3.G2) (all from Pharmingen), α_1 FITC (HMalpha1), β_4 PE (346-11A) (both from Serotec), α_L biotin (M17/4) (eBiosciences) and β_1 PE (HMbeta1-1) (BioLegend). The following isotype-matched antibody controls were employed: rat IgG2a PE (B39-4, R35-95), rat IgG1 PE (R3-34), hamster IgG2 FITC (Ha4/8), hamster IgM FITC (G235-1) (all Pharmingen), rat IgG2a biotin, rat IgG2b FITC (eB149/10H5), rat IgG1 FITC (all eBiosciences), hamster IgG PE (HTK888), hamster IgM biotin (HTK204) (both BioLegend) and rat IgG2a PE (YTH71.3) (Serotec). Biotinylated antibodies were detected with secondary streptavidin-Cy5 (Jackson). Flow cytometric analysis was performed with a FACScalibur and CellQuest Pro Software (BD Biosciences).

Quantitative RT–PCR. RNA was isolated from sorted DCs (see above) using the Absolutely RNA Microprep Kit (Stratagene) and the RNeasy Mini Kit (Qiagen). One microlitre cDNA, generated from 15 ng RNA using the iScript cDNA Synthesis Kit (Bio-Rad), was subjected to real-time PCR with the iQ SYBR Green Supermix (Bio-Rad) on the iCycler (Bio-Rad). Primers for integrin β_1 5′-AGACTTCCGCATTGGCTTTG-3′ and 5′-GCTGGTGCAGTTTTGTTCAC-3′, and integrin α_v 5′-CAAGCTCACTCCCATCAC-3′ and 5′-GGGTGTCTT-GATTCTCAAAGGG-3′ were used. Integrin gene expression in wild-type and $integrin^{-/-}$ DCs was quantified with the Gene Expression Analysis Program for the iCycler iQ Real-Time PCR Detection System (Bio-Rad). GAPDH was used to normalize gene expression, and integrin expression levels in wild-type DCs were set to 1.

***In vivo* migration assay.** Gr-1-depleted wild-type and $integrin^{-/-}$ DCs were labelled with 3.5 μM cell-permeable 5-(and-6)-carboxyfluorescein succinimidyl ester (CFSE) or 1 μM tetramethylrhodamine (TAMRA) (both Invitrogen), respectively, and vice versa (the fluorescent labels did not influence DC migration (not shown)). 1×10^6 DCs at a 1:1 ratio were suspended in 20 μl PBS and injected subcutaneously into the hind footpads of C57BL/6 mice. 32 and 48 h after injection, mice were killed by CO_2 suffocation, popliteal lymph nodes frozen in cryomatrix (Thermo) and sectioned in 12 μm slices. To visualize the

lymph node compartments, methanol-fixed cryosections were stained after blocking with 1% BSA in PBS with pan-laminin antibody (L9393, Sigma) and secondary anti-rabbit Cy5 (Jackson). Three different layers of the T cell cortex of each lymph node were documented using an Axio Imager upright microscope (Zeiss). Quantification of DCs within the T cell cortex was performed with MetaMorph (Molecular Devices). Using inverse thresholding, the greyscale images of both fluorescence channels were separately binarized. DCs appeared as dots that were quantified using the morphometric analysis tool. The ratio of migrated knockout DCs was calculated as the number of knockout cells divided by the total number of DCs in the T cell cortex, with 0.5 as the value where 50% of knockout cells and 50% wild-type cells located in the centre of the lymph node. To confirm that fluorescent cells in the lymph node represent DCs that migrated from the injection site (Supplementary Fig. 3), DCs were labelled with 3 μM Cell Trace Oregon Green 488 (Invitrogen). 1×10^6 DCs of either wild-type or integrin$^{-/-}$ DCs were injected as described above and 48 h later DCs were identified as green cells expressing CD86 by flow cytometric analysis.

***Ex vivo* wide-field microscopy in ear dermis.** Ears of killed C57BL/6 mice were removed and mechanically split into dorsal and ventral halves. During separation the dermis detached from the cartilage layer that remained on one of the halves. The cartilage free half was left unfixed and incubated with a rabbit polyclonal anti-LYVE-1 antibody (R&D Systems), washed with PBS and stained with a A488 conjugated anti-rabbit secondary antibody (Molecular Probes). The stained ears were mounted on custom-made migration chambers with the dermal surface exposed. LPS-matured BM-derived, MACS-purified, TAMRA-labelled DCs (see above) were re-suspended in culture medium, added on top of the dermis and incubated for 30 min at 37 °C, 5% CO_2. After gently washing away non-infiltrated DCs, the ear sheets were imaged in a custom-built climate chamber using a fully motorized upright Leica MZ 16 FA stereomicroscope equipped with a Spot camera and operated via MetaMorph software (system implemented by Visitron Systems). For multiple immunofluorescence stainings (Supplementary Fig. 5), ear sheets were fixed with 1% PFA after 120 min immigration of DCs and stained as described in the extravasation section. Cells were manually tracked using ImageJ as described below.

Two-photon intravital microscopy in lymph nodes. Intravital microscopy was performed as described previously[43]. Briefly, BM-derived DCs were matured overnight with LPS, purified and selected by MACS for the desired integrin deficiency (see above), differentially labelled with TAMRA and CFSE and subcutaneously injected into footpads of C57BL/6 mice. After 32 h popliteal lymph nodes were surgically exposed and imaged using an upright Leica DM LFSA microscope equipped with a ×20 0.95 NA water immersion objective (Olympus) and a MaiTai Ti:sapphire-pulsed laser (Spectra-Physics). 3D cell tracking was performed using Imaris software (Bitplane) as described.

***In vivo* ear irritation in bone marrow chimaeric mice.** BM chimaera of talin1$^{flox/flox}$, Mx1Cre$^{+/-}$ and $\alpha_v^{flox/flox}$, $\beta_1^{flox/flox}$, $\beta_2^{-/-}$, $\beta_7^{-/-}$, Mx1Cre$^{+/-}$ animals were generated by sublethal irradiation of wild-type mice and immediate reconstitution with 1×10^6 suspended BM cells of the indicated genotype. Six weeks after irradiation Poly (I)·Poly (C) was injected and 10 d later 20 μl of 1% croton oil (Sigma) in acetone[44] was applied on mouse ears. Mice were killed 12 h after application of croton oil. For histological analysis dorsal and ventral halves of ears were subjected to whole mount immunostaining. After fixation with 1% PFA, ear halves were blocked with 1% BSA (PAA) in PBS for 1 h at RT (while shaking), stained with anti-Gr-1 (RB6-8C5, Pharmingen) and anti-pan-laminin antibody (L9393, Sigma) in 1% BSA in PBS overnight at 4 °C (while shaking) and washed with 1% BSA in PBS. Primary antibodies were detected with a repeated cycle of staining with anti-rabbit A488 (Molecular Probes) and anti-rat Cy3 (Dianova) antibodies before tissue was embedded in elvanol and representative images taken with an Axio Imager (Zeiss) equipped with the Apotome. Concentration of granulocytes in blood was measured by staining peripheral blood with Gr-1 PE (BD Pharmingen) and counting all granulocytes per blood sample by flow cytometry using a FACSCalibur (BD Pharmingen). The numbers of granulocytes that extravasated into ear dermis were quantified by morphometric analysis employing MetaMorph imaging software (Molecular Devices).

3D collagen gel chemotaxis assay. For standard assays, PureCol (INAMED) in 1× minimum essential medium eagle (MEM, Sigma) and 0.4% sodium bicarbonate (Sigma) was mixed with cells in RPMI (Invitrogen), 10% fetal calf serum (FCS, Invitrogen) at a 2:1 ratio, resulting in gels with a collagen concentration of 1.6 mg ml^{-1}. Final cell concentrations in the assay were 1×10^6 cells per ml gel for DCs and 1.6×10^6 cells per ml gel for granulocytes and B lymphoblasts. For collagen titration experiments, above ratios were adapted. For gels with 3–5 mg ml^{-1} collagen concentration, Nutragen (INAMED) was employed. Collagen-cell mixtures were cast in custom-made migration chambers with a thickness of 0.5–1 mm. After 30 min assembly of the collagen fibres at 37 °C, the gels were overlaid with 50 μl of the following recombinant chemokines (all R&D Systems) diluted in RPMI, 10% FCS: CCL19 (0.6 μg ml^{-1}, DCs), C5a (0.1 μg ml^{-1}, granulocytes) and CXCL13 (2.5 μg ml^{-1}, B cells). For inhibition studies, leukocytes were pre-incubated for 30 min with 50 μM blebbistatin (Sigma), 30 μM Y27632, 100 nM or 500 nM latrunculin B (both Calbiochem) before casting the gels. Inhibitors were also present in the same end-concentrations in the gel.

3D fibrin gel chemotaxis assay. Cells were taken up in 0.2% (w/v) human fibrinogen (IMCO) in RPMI, 10% FCS to a final concentration of 1×10^6 cells per ml gel. Before casting the gels in custom-made migration chambers, 0.125 U ml^{-1} thrombin (Calbiochem) was added. After 30 min polymerization of the fibrin gels at 37 °C, the gels were overlaid with 50 μl of 0.6 μg ml^{-1} CCL19 (R&D Systems) in RPMI, 10% FCS.

Analysis of chemotaxis assays. For comparison of DC velocities in collagen and fibrin gel assays in the absence of inhibitors (Fig. 3b and Supplementary Fig. 7a), movies were converted to kymographs using MetaMorph imaging software. Straight lines in the kymographs represent migrating cells and lead angles were measured to calculate single cell velocities. Manual single cell tracking of random samples employing ImageJ and the Manual Tracking Plugin revealed the same results. Manual tracking was applied to all other 3D chemotaxis assays. Here cells were tracked over 4 h (for DCs, 2 min per frame) or 15 min (for granulocytes, 15 s per frame). Speed and directionality parameters were calculated and visualized as plots and movies by analysing the acquired data with the Chemotaxis and Migration Tool Plugin (http://www.ibidi.de/applications/ap_chemo.html). For quantification of ''resting'' and ''moving'' phases in 0.75 mg ml^{-1} collagen gels (Supplementary Fig. 9) instantaneous velocities (distance per 2 min) were categorized as ''resting'' if velocity <1 μm per 2 min and ''moving'' if velocity ≥ 1 μm per 2 min. Average velocities during mobile phases were calculated by excluding the resting fraction. The percentage of resting phases was calculated as resting time / (resting time + moving time).

Time-lapse video microscopy. Low magnification bright-field movies of DCs in gels were recorded in indicated time intervals using inverted Axiovert 40 (Zeiss) cell culture microscopes, equipped with custom-built climate chambers (5% CO_2, 37 °C, humidified) and PAL cameras (Prosilica) triggered by custom-made software (SVS Vistek). High magnification DIC and fluorescence movies were recorded using a fully automated Axiovert 200M inverted fluorescence microscope with a 40× objective (Zeiss) and a CoolSNAP HQ CCD camera. The microscopic set-up (Visitron Systems) was controlled by MetaMorph software.

Transfection and labelling of cells. DCs were transfected with MLC-GFP (gift of M. Olson[45]) between days 8–10 of culture using the primary mouse T cell kit and the Amaxa nucleoporator (Amaxa). Cells were transfected according to the manufacturer's recommendations and immediately after transfection LPS was added for overnight maturation. For nucleus visualization of DCs and granulocytes nucleic acid dyes SYTO11 and SYTO13 (Invitrogen) were used, respectively, according to the manufacturers recommendations.

2D adhesion assays. Adhesion assays were performed in 24-well plates coated with 10 μg ml^{-1} fibronectin (Calbiochem) or 10 μg ml^{-1} recombinant mouse ICAM-1 (R&D). 3×10^5 DCs per well were seeded in RPMI medium containing 10% FCS in the presence of 200 ng ml^{-1} LPS and incubated for 30 min at 5% CO_2, 37 °C. Same cell numbers of LPS-maturated DCs were seeded in the presence of 200 ng ml^{-1} phorbol 12-myristate 13-acetate (Calbiochem) for 30 min. Cells were washed manually 3 times with PBS, 1% BSA and subsequently photo-documented and counted manually. Time-lapse video microscopy of chemokine-induced spreading of LPS-matured DCs (see Supplementary Video 4) was performed on 10 μg ml^{-1} mouse CCL21 (R&D)-coated plastic of cell culture dishes.

37. Bader, B. L., Rayburn, H., Crowley, D. & Hynes, R. O. Extensive vasculogenesis, angiogenesis, and organogenesis precede lethality in mice lacking all alpha v integrins. *Cell* **95**, 507–519 (1998).
38. Nagy, A., Rossant, J., Nagy, R., Abramow-Newerly, W. & Roder, J. C. Derivation of completely cell culture-derived mice from early-passage Embryonic stem cells. *Proc. Natl Acad. Sci. USA* **90**, 8424–8428 (1993).
39. Schaft, J., Ashery-Padan, R., van der Hoeven, F., Gruss, P. & Stewart, A. F. Efficient FLP recombination in mouse ES cells and oocytes. *Genesis* **31**, 6–10 (2001).
40. Bungartz, G. *et al.* Adult murine hematopoiesis can proceed without beta1 and beta7 integrins. *Blood* **108**, 1857–1864 (2006).
41. Lutz, M. B. *et al.* An advanced culture method for generating large quantities of highly pure dendritic cells from mouse bone marrow. *J. Immunol. Methods* **223**, 77–92 (1999).
42. Fässler, R. & Meyer, M. Consequences of lack of beta 1 integrin gene expression in mice. *Genes Dev.* **9**, 1896–1908 (1995).
43. Worbs, T., Mempel, T. R., Bolter, J., von Andrian, U. H. & Förster, R. CCR7 ligands stimulate the intranodal motility of T lymphocytes *in vivo*. *J. Exp. Med.* **204**, 489–495 (2007).
44. Berg, D. J. *et al.* Interleukin 10 but not interleukin 4 is a natural suppressant of cutaneous inflammatory responses. *J. Exp. Med.* **182**, 99–108 (1995).
45. Croft, D. R. *et al.* Actin-myosin-based contraction is responsible for apoptotic nuclear disintegration. *J. Cell Biol.* **168**, 245–255 (2005).